DYNAMICS OF GALAXIES

8. Dynamics of elliptical galaxies

Piet van der Kruit
Kapteyn Astronomical Institute
University of Groningen
the Netherlands

Winter 2008/9

Fundamental Plane

With Fish's law (constant central surface brightness) and constant M/L then follows the Faber-Jackson relation[1] between luminosity L and stellar velocity dispersion σ:

$$L \propto \sigma^4$$

This is equivalent to the Tully-Fisher relation for spirals.

There is also a relation between diameter D_Σ (the radius at which the mean surface brightness is 20.75 mag arcsec^{-2}) and the velocity dispersion[2]:

$$D_\Sigma \propto \sigma^{4/3}$$

[1] S.M. Faber & R.E. Jackson, Ap.J. 204, 668 (1976)
[2] A. Dressler *et al.*, Ap.J. 313, 42 (1987)

This can be used to decrease the scatter in the FJ-relation by including surface brightness ($\langle SB_{\rm e} \rangle$ = mean surface brightness within the effective radius) as a second parameter

$$L \propto \sigma^{2.65} \langle SB_{\rm e} \rangle^{-0.65}.$$

The "fundamental plane" of elliptical galaxies is a relation between some consistently defined radius (e.g. core radius) R, the observed central velocity dispersion σ and a consistently defined surface brightness I[3]:

$$R \propto \sigma^{1.4 \pm 0.15} I^{-0.9 \pm 0.1}$$

[3] see J. Kormendy & G. Djorgovski, Ann.Rev.Astron.Astrophys. 27, 235 (1989)

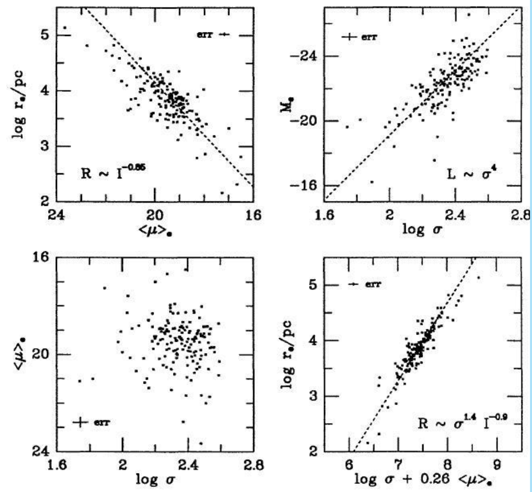
log r$_e$/pc
<μ>$_e$
err
R ~ I$^{-0.85}$
M$_e$
log σ
L ~ σ^4
R ~ σ$^{1.4}$ I$^{-0.9}$
log σ + 0.26 <μ>$_e$

In broad terms the Fundamental Plane can be understood as follows.

For equilibrium the Virial Theorem states that

$$2T_{\rm k} + \Omega = 0$$

where $T_{\rm k}$ is the total kinetic energy and Ω the potential energy.

The kinetic energy is proportional to MV^2 and the potential energy to M^2/R. Here M is the total mass, V a typical internal velocity and R some characteristic radius.

All the information on the detailed density and velocity structure is in the proportionality constants.

Thus we have

$$M \propto RV^2$$

For elliptical galaxies the kinetic energy is dominated by that in random motions rather then rotation. So for V we will take the mean velocity dispersion[4] σ.

With the mass-to-light ratio M/L, we replace M with $L(M/L)$ with L the total luminosity. For R we take a typical radius such as the effective radius; then we get

$$R \propto L \left(\frac{M}{L} \right) \sigma^2$$

[4] If σ is the observed line-of-sight velocity dispersion, the typical velocity is actually the three-dimensional velocity dispersion 3σ.

If I is the mean surface brightness within R we have $I \propto LR^{-2}$ and

$$R \propto \sigma^2 I^{-1} \left(\frac{M}{L}\right)^{-1}$$

The observed FP was

$$R \propto \sigma^{1.4\pm0.15} I^{-0.9\pm0.1}$$

The coefficients are close to the observed ones. Differences arise because of variations in actual structural parameters and possible dependence of M/L on M and/or σ.

Rotation and shapes

Flattening of oblate spheroids

If we consider elliptical galaxies to be oblate spheroids, flattened by rotation we can estimate how much rotation is needed using the virial equation.

Let the spheroid be flattened along the z-axis. Then the symmetry with respect to this axis requires

$$\langle V_{\rm R} \rangle = \langle V_{\rm z} \rangle = \langle V_{\rm R} V_\theta \rangle = \langle V_{\rm z} V_\theta \rangle = 0$$

The rotational velocity is $\langle V_\theta \rangle$.

Start with the motions tensor

$$T_{ij} = \frac{1}{2} \int \bar{v}_i . \bar{v}_j d^3 x$$

We have

$$\langle v_{\rm x} \rangle = \langle V_\theta \rangle \sin\theta \quad ; \quad \langle v_{\rm y} \rangle = \langle V_\theta \rangle \cos\theta$$

Then

$$\begin{aligned} T_{\rm xy} &= \tfrac{1}{2} \int \rho \langle v_{\rm x} \rangle \langle v_{\rm y} \rangle d^3x \\ &= \tfrac{1}{2} \int_0^{2\pi} \int_0^{\infty} \int_{-\infty}^{\infty} \rho(R,z) \langle V_\theta \rangle^2 \sin\theta \cos\theta \; dz \; dR \; d\theta \\ &= 0 \end{aligned}$$

since

$$\int_0^{2\pi} \sin\theta \cos\theta d\theta = \tfrac{1}{2} \int_0^{2\pi} \sin(2\theta) d\theta = \tfrac{1}{2} \sin^2(\theta) \Big|_0^{2\pi} = 0$$

Similarly, *all* non-diagonal elements of the tensors T_{ij}, Π_{ij} and W_{ij} can be shown to be equal to zero.

Them because of symmetry in the system we must also have

$$T_{xx} = T_{yy} \quad ; \quad \Pi_{xx} = \Pi_{yy} \quad ; \quad W_{xx} = W_{yy}$$

So the only non-trivial virial equations are

$$2T_{xx} + \Pi_{xx} + W_{xx} = 0 \quad ; \quad 2T_{zz} + \Pi_{zz} + W_{zz} = 0$$

So

$$\frac{2T_{xx} + \Pi_{xx}}{2T_{zz} + \Pi_{zz}} = \frac{W_{xx}}{W_{zz}}$$

The ratio W_{xx}/W_{zz} for density distributions with surfaces of equal density being confocal ellipsoids can be shown to be independent of the actual radial dependence of the density. I illustrate that now.

Assume that the axis ratio is c/a and therefore the excentricity

$$e = \sqrt{1 - \frac{c^2}{a^2}}$$

Let the density along the major axis be $\rho(R)$. Define

$$\alpha(R,z) = R^2 + \frac{z^2}{1-e^2}$$

Then inside the spheroid with radius a the forces and potential are

$$K_{\rm R} = -\frac{4\pi G\sqrt{1-e^2}}{e^3} R \int_0^{\sin^{-1} e} \rho(\alpha) \sin^2\beta d\beta$$

$$K_{\rm z} = -\frac{4\pi G\sqrt{1-e^2}}{e^3} z \int_0^{\sin^{-1} e} \rho(\alpha) \tan^2\beta d\beta$$

$$\Phi(R,z) = \frac{4\pi G\sqrt{1-e^2}}{e}\left[\int_0^{\delta} \rho(\alpha)\alpha\beta d\alpha + \sin^{-1} e \int_{\delta}^{a} \rho(\alpha)\alpha d\alpha\right]$$

Here

$$\delta^2 = R^2 + \frac{z^2}{1-e^2}$$

and

$$\alpha^2 = \frac{R^2 \sin^2\beta + z^2 \tan^2\beta}{e^2}$$

With partial integration we may write in the equation for $K_{\rm R}$

$$\int_0^{\sin^{-1} e} \rho \sin^2 \beta d\beta = \rho B_1 - \int_0^{\sin^{-1} e} \frac{\partial \rho}{\partial \beta} d\beta$$

with

$$B_1 = \int_0^{\sin^{-1} e} \sin^2 \beta d\beta = \tfrac{1}{2}(\beta - \sin\beta \cos\beta)\Big|_0^{sin^{-1} e}$$

This is a constant and then

$$K_{\rm R} = -\frac{4\pi G\sqrt{1-e^2}}{e^3} R B_1 \left[\rho - \int_0^{\sin^{-1} e} \frac{\partial \rho}{\partial \beta} d\beta \right]$$

Similarly

$$K_{\rm z} = -\frac{4\pi G\sqrt{1-e^2}}{e^3} z B_2 \left[\rho - \int_0^{\sin^{-1} e} \frac{\partial \rho}{\partial \beta} d\beta \right]$$

with

$$B_2 = \int_0^{\sin^{-1} e} \tan^2 \beta d\beta = (-\beta + \tan \beta)|_0^{sin^{-1}e}$$

Now remember that

$$W_{RR} = -\int R \frac{\partial \Phi}{\partial R} d^3x = \int R K_{\rm R} d^3x$$

$$W_{zz} = -\int z \frac{\partial \Phi}{\partial z} d^3x = \int z K_{\rm z} d^3x$$

So in the ratio W_{xx}/W_{zz} the dependence on the functional form of ρ disappears[5].

In fact, to a good approximation, for oblate bodies we have then

$$\frac{2T_{xx} + \Pi_{xx}}{2T_{zz} + \Pi_{zz}} = \frac{W_{xx}}{W_{zz}} \propto \left(\frac{c}{a}\right)^{-0.9}$$

Now consider the cases where the system is either rotating or not or has an isotropic or anisotropic velocity distribution.

[5] The actual ratio is related to parameters in Table 2-1 of Binney & Tremaine.

A. Isotropic and rotating.

Then the velocity dispersion σ is independent of direction. But it may vary with the ellipsoidal surface it is on and therefore we use a density-weighted rms (one-dimensional) velocity dispersion $\bar{\sigma}$. So, if the total mass is M

$$\Pi_{xx} = \int \rho \sigma_{xx}^2 d^3x = M\bar{\sigma}^2 = \Pi_{zz}$$

Say, the density-weighted rotation velocity (around the z-axis) is $\bar{V}$; then $v_x^2 = \frac{1}{2}\bar{V}^2$, and we get

$$T_{zz} = 0$$

$$T_{xx} = \frac{1}{2}\int \rho v_x^2 d^3x = \frac{1}{4}M\bar{V}^2 = T_{yy}$$

Therefore

$$\frac{\frac{1}{2} M \bar{V}^2 + M \bar{\sigma}^2}{M \bar{\sigma}^2} = \left(\frac{c}{a} \right)^{-0.9}$$

This can be reduced to

$$\frac{\bar{V}}{\bar{\sigma}} = \sqrt{2 \left[\left(\frac{c}{a} \right)^{-0.9} - 1 \right]}$$

This is interesting, since it shows that a large amount of rotation is necessary to give rise to flatterning. E.g. for a rather modest flattening of $c/a = 0.7$ one needs $\bar{V} \sim 0.9\bar{\sigma}$.

B. Anisotropic and non-rotating

Then $T_{xx} = 0$ and $\Pi_{xx} = M\bar{\sigma}_{xx}^2$, $\Pi_{zz} = M\bar{\sigma}_{zz}^2$

This gives

$$\frac{\bar{\sigma}_{zz}}{\bar{\sigma}_{xx}} \sim \left(\frac{c}{a}\right)^{-0.9}$$

For the same modest flattening of $c/a = 0.7$ one now needs only a small anisotropy $\bar{\sigma}_{zz}/\bar{\sigma}_{xx} \sim 0.85$.

C. Anisotropic and rotating

Write

$$\Pi_{zz} = (1-\delta)\Pi_{xx} = (1-\delta)M\bar{\sigma}^2$$

We have again $T_{zz} = 0$ and $2T_{xx} = \frac{1}{2}M\bar{V}^2$.

Then

$$\frac{\bar{V}}{\bar{\sigma}} = \sqrt{2\left[(1-\delta)\left(\frac{c}{a}\right)^{-0.9} - 1\right]}$$

This would mean that we can expect a relation between $\bar{V}/\bar{\sigma}$ and the ellipticity $\epsilon = 1 - (c/a)$ in elliptical galaxies.

However, we observe these systems from random orientations and see an apparent flattening, a projected rotation and the integrated velocity dispersion along the line-of-sight.

It turns out that this only shifts the galaxies that are oblate, isotropic rotators in the *apparent* $(V_{\rm m}/\bar{\sigma} - \epsilon)$-plane roughly along the line of the correlation[6].

So we can compare the observations with the predictions from the anisotropic, rotating case.

[6] See Binney & Tremaine, section 4.3 (page 217)

$V_{\rm m}/\bar{\sigma} - \epsilon$ relation and triaxiality

Originally elliptical galaxies were thought to be simple systems, mainly supported by random motions and flattened by rotation.

The rotation turned out to be too small to provide the flattening so this had to be due to anisotropic velocity distributions.

A parameter used is the ratio of the observed (projected) maximum rotation velocity $V_{\rm m}$ and the observed line-of-sight velocity dispersion at the center $\bar{\sigma}$.

This is a measure of the relative importance of rotation and random motions.

It can be compared to the observed flattening $\epsilon = 1 - b/a$ with a and b the (projected) major and minor axis[7].

The symbols in the next graph indicate models with isotropic velocity dispersions that are flattened by rotation and seen under various inclinations.

The bars are data and rotate less than expected for the observed flattening.

Note that the models lie on a well-defined line where the intrinsic relation roughly coincides with the projected one.

[7] G. Illingworth, Ap.J. 218, L43 (1977)

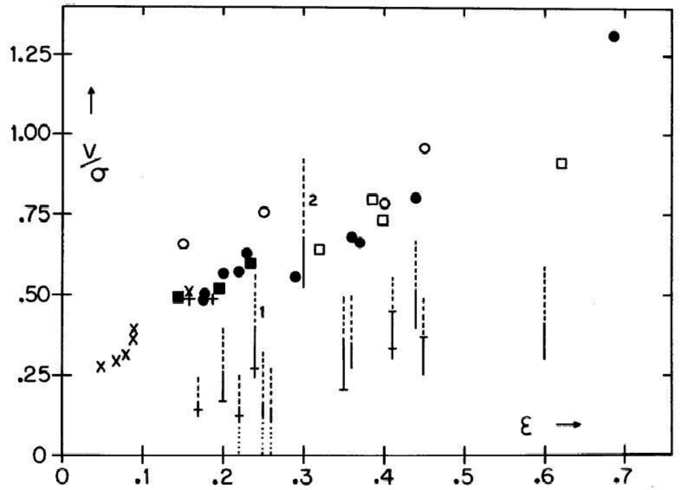
1.25
1.00
.75
.50
.25
0
V/σ
2
1
ε
0
.1
.2
.3
.4
.5
.6
.7

Further work[8] showed that spiral bulges and faint ellipticals are fast rotators.

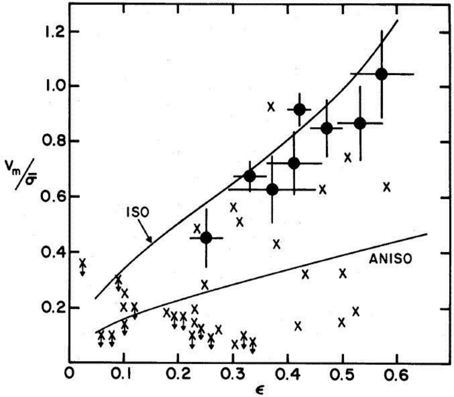

FIG. 3.—Comparison of bulge data (*filled circles*) with all available elliptical galaxy data (*crosses*, *arrows* indicate upper limits) in the dimensionless rotation-ellipticity plane. Derivation of V_m, $\bar{\sigma}$, and ε is discussed in the text. The line labeled ISO represents projected models of oblate spheroids with isotropic residual velocities and rotational flattening. The line labeled ANISO describes a typical anisotropic oblate model with σ_z smaller than σ_r and σ_θ.

[8] e.g. J. Kormendy & G. Illingworth, Ap.J. 256, 460 (1982)

Minor axis rotation was first discovered in NGC 4261[9].

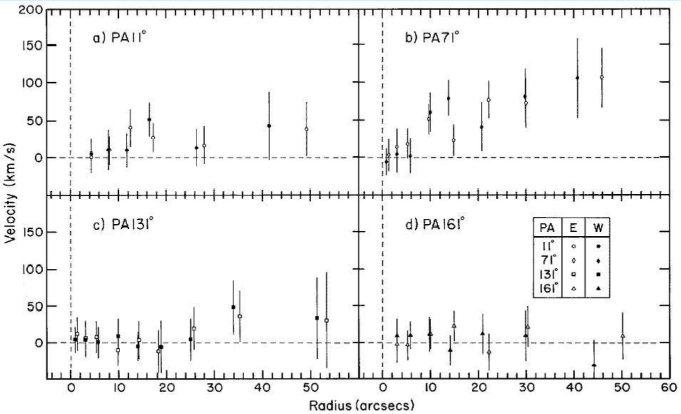

[9] R.L. Davies & M. Birkinshaw, Ap.J. 303, L45 (1986)

The maximum rotation is in p.a. $\sim 70^\circ$, while the isophotes have major axis at $\sim 160^\circ$.

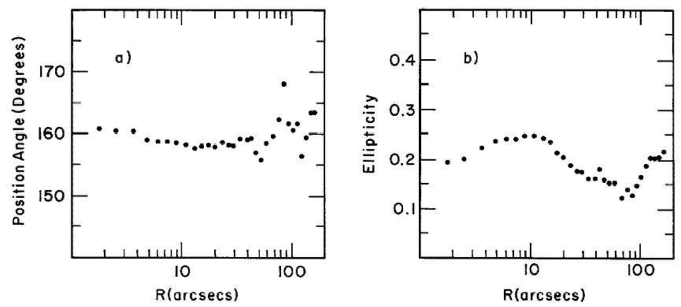

The suggestion was made that this galaxy is prolate.

It turned out that elliptical galaxies are triaxial[10].

This explains the $(V_{\rm m}/\sigma - \epsilon)$-relation, the isophote twists and the minor axis rotation.

Minor axis rotation can result from[11]:

- projection effects in triaxial systems or
- misalingment of the angular momentum and the shortest axis.

---

[10] J. Binney, Mon.Not.R.A.S. 183, 779 (1978)
[11] M. Franx, G. Illingworth & P.T. de Zeeuw, Ap.J. 383, 112 (1991)

Define the misalignment $\psi_{\rm int}$ as the angle between the intrinsic short axis and the angular momentum.

Define for axes $a \geq b \geq c$ the triaxiality

$$T = \frac{a^2 - b^2}{a^2 - c^2} = \frac{1 - b^2/a^2}{1 - c^2/a^2}$$

Thus $T=0$: oblate; $T=1$: prolate.

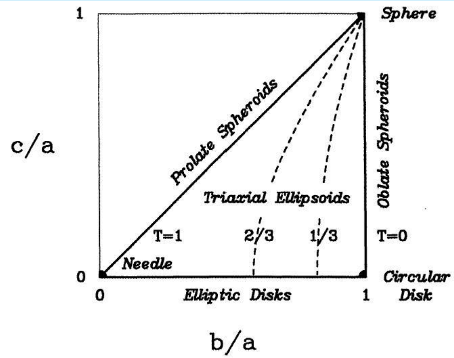

We can *measure* the apparent ellipticity ϵ and the apparent misalignment ψ (the ratio of maximum observed velocity on the apparent axes)

$$\tan\psi = \frac{v_{\rm min}}{v_{\rm maj}}.$$

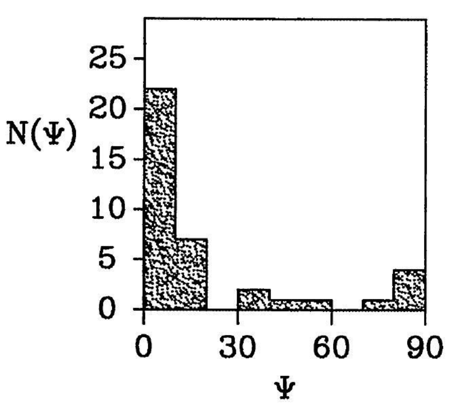

The distributions observed give the following rough indications:

- Most (at least 50%) ellipticals have a small $\psi_{\rm int}$ ($\lesssim 10^\circ$), but some ($\approx$ 10%) rotate along their major axis.
- $\langle T \rangle \approx 0.3$ and T has a wide distribution with possibly as much as 40% of the galaxies prolate.
- The ratio c/a has a peak at about 0.6-0.7.

Dust lanes are often seen[12] and occur usually along the apparent minor axis, but also sometimes along the major axis.

[12] F. Bertola & G. Galletta, Ap.J. 226, L115 (1978)

Here is NGC 1947.

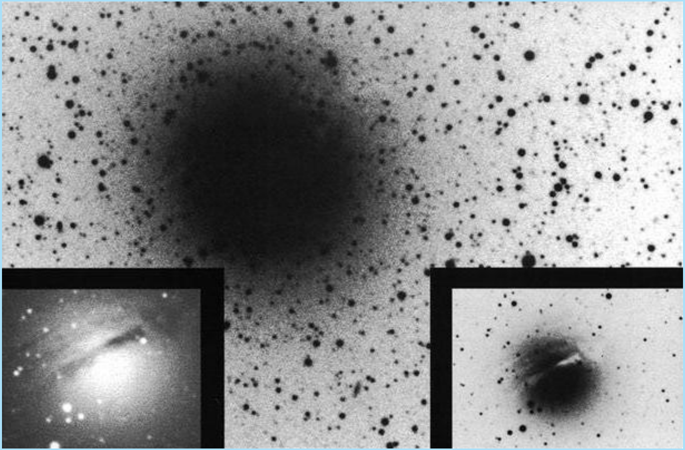

In triaxial potentials stable orbits are possible, but the detailed kinematics depends on the galaxy shape and body rotation.

In principle dust lanes can be used to determine the intrinsic shape of an individual galaxy [13].

[13] R.L. Merritt & P.T. de Zeeuw, Ap.J. 267, L19 (1983); J. Kormendy & G. Djorkovski, Ann.Rev.A&A. 27, 235 (1989)

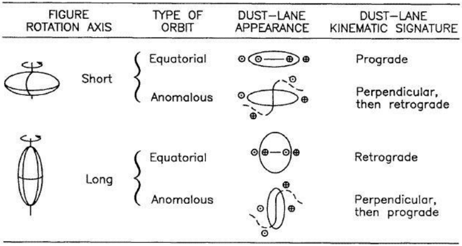

Figure 1 Stable orbits of gas in a rotating triaxial galaxy (adapted from Merritt & de Zeeuw 1983). As illustrated, the figure tumbles in the direction of stellar rotation ($\Omega_p > 0$); if $\Omega_p < 0$, the sense of gas rotation is reversed. Assume that the figure rotates about its shortest or longest axis (*left*). The second column gives the kind of orbit, and the third sketches resulting dust lanes seen edge-on. Anomalous orbits have different orientations at different radii (van Albada et al. 1982). They are the analogues of polar orbits in a stationary potential; at small radii, where Ω_p is unimportant, they are polar. At large radii, the figure rotates several times during an orbit and so is effectively oblate-spheroidal; then the orbit is equatorial (Simonson 1982). In between, the orbits have skew orientations determined by the Coriolis force. The schematic illustrations of dust lanes show the directions of stellar and gas motion; $\odot$ indicates approach, and $\oplus$ indicates recession. The right column states the kinematic signature, i.e. the sense of rotation of the dust lane with respect to the stars.

Detailed kinematics

Detailed kinematics, including higher order moments of the velocity distyribution, of the velocity distributions can now be observed very well.

An example is a study of NGC3379[14].

Dynamical modeling shows that NGC 3379 may be a flattened, weakly triaxial system seen in an orientation that makes it appear round.

[14] T.S. Statler & T. Smecker-Hane, A.J. 117, 839 (1999)

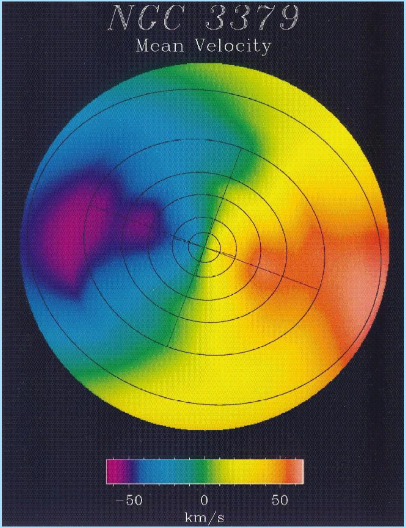
NGC 3379
Mean Velocity
−50 0 50
km/s

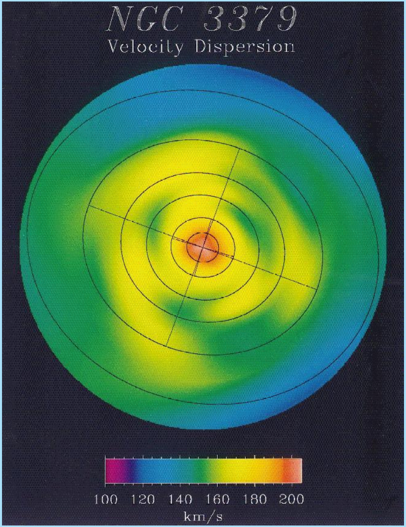
NGC 3379
Velocity Dispersion
100 120 140 160 180 200
km/s

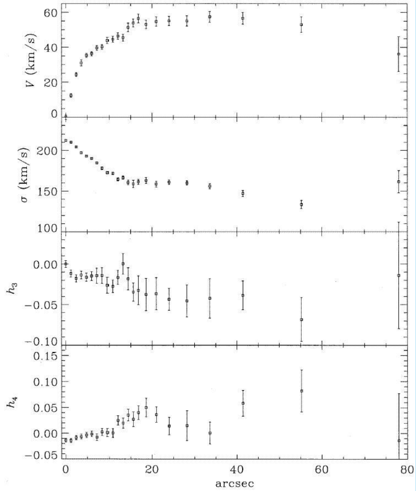
60
40
20
0
V (km/s)
200
150
100
σ (km/s)
0.00
−0.05
−0.10
h_3
0.15
0.10
0.05
0.00
−0.05
h_4
0
20
40
60
80
arcsec

Recently the SAURON integral field spectrograph has been built and used to survey kinematics and structure of elliptical galaxies[a].

[a] P.T. de Zeeuw et al., Mon.Not.R.A.S. 329, 513 (2002)

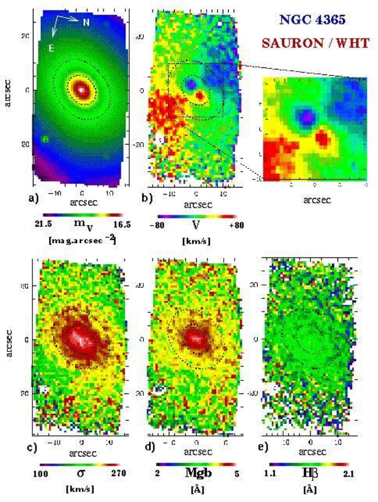

Central kinematics and black holes

The central regions often show kinematics deviating from the outer parts.

These distinct cores may show:

- Rapid rotation in the core but slow rotation in the main body
- Opposite rotation in the core relative to that in the main body
- Core rotation along the minor axis.

The distinct cores usually show small velocity dispersions, which suggest a two-component galaxy consisting of an elliptical with a small central disk.

Evidence for black holes comes from rapid rotation and high velocity dispersions in the inner regions, such as in NGC 4594[15] or our own Galaxy.

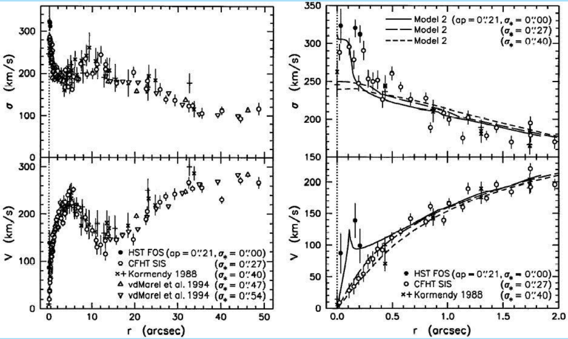

[15] J. Kormendy et al., Ap.J. 473, L91 (1996)

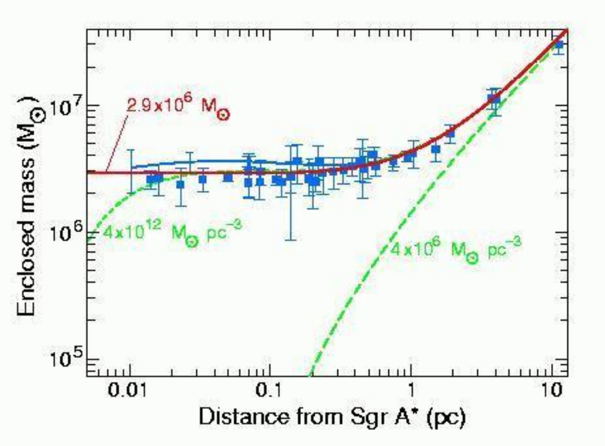
Enclosed mass ($M_\odot$)
10^7
10^6
10^5
$2.9 \times 10^6\ M_\odot$
$4 \times 10^{12}\ M_\odot\ pc^{-3}$
$4 \times 10^6\ M_\odot\ pc^{-3}$
0.01
0.1
1
10
Distance from Sgr A* (pc)

A compilation of all available data[16] shows a tight correlation between the mass of the black hole and the luminosity or velocity dispersion in the main body of the elliptical galaxy or bulge.

Probably this means no more than that larger galaxies have more material to feed into the center.

[16] S. Tremaine et al., Ap.J. 574, 740 (2002)

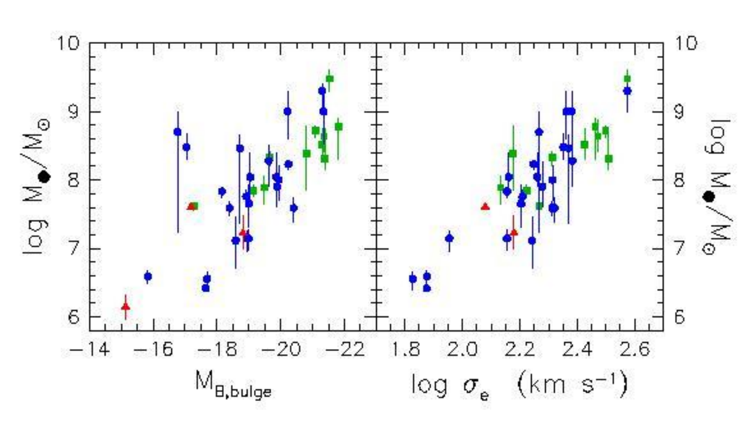
log $M_\bullet / M_\odot$
10
9
8
7
6
−14
−16
−18
−20
−22
$M_{B,\mathrm{bulge}}$
1.8
2.0
2.2
2.4
2.6
log σ_e (km s^{-1})

Dynamical models and dark matter

Stäckel potentials

The most simple description of an elliptical is that of King models, which are isothermal spheres with tidal radii and truncations in the velocity distributions. For these we have can estimate the total mass from

$$\frac{M}{L} = \frac{9\sigma^2}{2\pi G I_0 r_{\rm c}}.$$

However, we have seen that ellipticals have anisotropic velocity distribrutions and are in general triaxial.

A describtion then is with Stäckel potentials, which are potentials that are separable in ellipsoidal coordinates.

These are coordinates (λ, μ, ν) that are the three roots of τ for

$$\frac{x^2}{\tau+\alpha} + \frac{y^2}{\tau+\beta} + \frac{z^2}{\tau+\gamma} = 1$$

with $\alpha \leq \beta \leq \gamma$ three constants. It then turns out that

$$-\gamma \leq \nu \leq -\beta \leq \mu \leq -\alpha \leq \lambda$$

The line element is $ds^2 = P^2 d\lambda^2 + Q^2 d\mu^2 + R^2 d\nu^2$ with

$$P^2 = \frac{(\lambda-\mu)(\lambda-\nu)}{4(\lambda+\alpha)(\lambda+\beta)(\lambda+\gamma)} \quad ; \quad Q^2 = \frac{(\mu-\nu)(\mu-\lambda)}{4(\mu+\alpha)(\mu+\beta)(\mu+\gamma)}$$

$$R^2 = \frac{(\nu-\lambda)(\nu-\mu)}{4(\nu+\alpha)(\nu+\beta)(\nu+\gamma)}$$

In such coordinate systems surfaces of constant λ are ellipsoids, of constant μ hyperboloids of one sheet and of constant ν hyperboloids of two sheets.

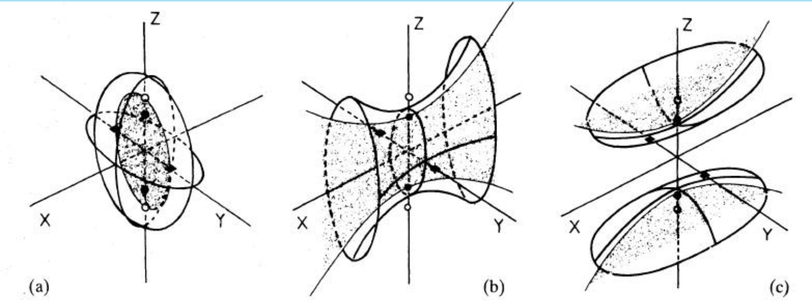

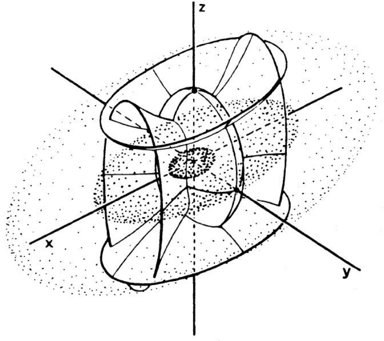
z
x
y

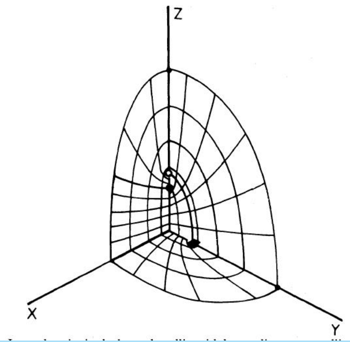
Z
X
Y

Stäckel potentials are of the form

$$\Phi(\lambda,\mu,\nu) = -\frac{F(\lambda)}{(\lambda-\mu)(\lambda-\nu)} - \frac{F(\mu)}{(\mu-\nu)(\mu-\lambda)} - \frac{F(\nu)}{(\nu-\lambda)(\nu-\mu)}$$

This can be used to describe triaxial galaxies[17].

Many density distributions can be locally approximated with a Stäckel potential.

For example, it is possible to derive a local approximation to the the potential in a disk with a flat rotation curve by a Stäckel potential[18].

[17] P.T. de Zeeuw & D. Lynden-Bell, Mon.Not.R.A.S. 215, 713 (1985); P.T. de Zeeuw, Mon.Not.R.A.S. 216, 273 (1985)

[18] T.S. Statler, Ap. J. 344, 217 (1989)

If the density is specified on the z-axis and if the potential is of the Stäckel-form in a specified ellipsoidal coordinate system, then the density at any point can be calculated with the so-called generalized Kuzmin formula[19].

A set of models with simple density profiles has been calculated[20] to illustrate the usefulness.

A nice example is the modified Hubble model, which has

$$\rho(z) = \rho_\circ (1 + z^2)^{-3/2}$$

Then the coordinate system determines what the axis ratio's are in the density distributions and these change with radius.

[19] P.T. de Zeeuw, Mon.Not. R.A.S. 216, 599 (1985)

[20] P.T. de Zeeuw, R. Peletier & M. Franx, Mon.Not.R.A.S. 221, 1001 (1986)

Here are isodensity curves for a typical triaxial modified Hubble model (contour interval $\log 3$).

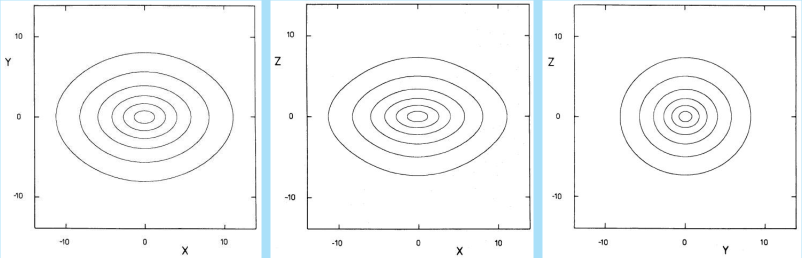

So, this density distribution has smooth isodensity surfaces <u>and</u> has in a potential of Stäckel form!

The perfect ellipsoid

Every orbit in a Stäckel potential is the sum of three motions, one in each coordinate.

As a result motion is bounded by coordinate surfaces.

It is of use to study the types of orbits that arise in triaxial potentials.

A beautiful illustration is the case of the perfect ellipsoid[21], which is both stratified on concentric (triaxial) ellipsoids and produces exactly a Stäckel potential.

[21] P.T. de Zeeuw, Mon.Not.R.A.S. 216, 273 (1985)

The perfect ellipsoid has the density distribution

$$\rho = \frac{\rho_\circ}{(1+\tilde{m}^2)^2} \quad ; \quad \tilde{m}^2 = \frac{x^2}{a^2} + \frac{y^2}{b^2} + \frac{z^2}{c^2} \quad ; \quad a \geq b \geq c$$

This has semi-axes $\tilde{m}a$, $\tilde{m}b$ and $\tilde{m}c$ and falls off as $\tilde{m}^{-4}$ at large distances.

The function $F(\tau)$ in the equation for the potential then is

$$F(\tau) = \pi G \rho_\circ abc(\tau+\alpha)(\tau+\gamma) \int_0^\infty \frac{\sqrt{u-\beta}}{\sqrt{(u-\alpha)(u-\gamma)}} \frac{du}{u+\tau}$$

There are exact solutions for the (isolating) integrals of motion:

$$H = X + Y + Z$$

$$J = (\mu + \nu)X + (\nu + \lambda)Y + (\lambda + \mu)Z$$

$$K = \mu\nu X + \nu\lambda Y + \lambda\mu Z$$

where

$$X = \frac{P^2\dot{\lambda}^2}{2} - \frac{F(\lambda)}{(\lambda - \mu)(\lambda - \nu)} \quad ; \quad Y = \frac{Q^2\dot{\mu}^2}{2} - \frac{F(\mu)}{(\mu - \nu)(\mu - \lambda)}$$

$$Z = \frac{R^2\dot{\nu}^2}{2} - \frac{F(\nu)}{(\nu - \lambda)(\nu - \mu)}$$

These integrals are all quadratic in velocity and have the dimension of an energy.

It is more insightfull to write the integrals as the energy (as usual) and two non-classical integrals:

$$I_1 = H$$

$$I_2 = \frac{\alpha^2 H + \alpha J + K}{\alpha - \gamma}$$

$$I_3 = \frac{\gamma^2 H + \gamma J + K}{\gamma - \alpha}$$

Special case I: the prefect prolate spheroid. Here $\gamma = \beta$ (so the long axis is the *x*-axis). Since

$$-\gamma \leq \nu \leq -\beta \leq \mu \leq -\alpha \leq \lambda$$

we have

$$\nu = -\gamma = \beta$$

The third integral then becomes the (classical) angular momemtum along the *x*-axis

$$I_3 = \tfrac{1}{2}(y\dot{z} - z\dot{y})^2 = \tfrac{1}{2}L_\mathrm{x}^2$$

The integral I_2 remains a non-classical one.

Special case II: the perfect oblate spheroid. Then we have $\mu = -\beta = -\alpha$.

In this case the angular momentum around the z-axis is an isolating integral:

$$I_2 = \frac{1}{2}(x\dot{y} - y\dot{x})^2 = \frac{1}{2}L_z^2$$

I_3 is the well-know third integral of Galactic dynamics.

I_3 remains a non-classical integral.

Special case III: If we collapse the perfect oblate spheroid along the symmetry axis we get the Kuzmin disk.

With $\mu = -\beta = -\alpha$ and $\gamma = 0$ we get the same I_2 as above and in addition

$$I_3 = \frac{1}{2} L_{\rm x}^2 + \frac{1}{2} L_{\rm y}^2 + \frac{1}{2} a\dot{z}^2 - a|z|\Phi$$

(a is the coordinate system focal distance above and below the plane)

I_3 has the property of an energy associated with the z-axis.

In this case we then have three isolating integrals E, I_2 and I_3.

Special case IV: the perfect sphere. Then $\mu = \nu = -\gamma = -\beta = -\alpha$. So

$$J = \tfrac{1}{2}L^2 - 2\alpha H \quad : \quad K = \alpha^2 - \tfrac{1}{2}\alpha L^2 \quad ; \quad I_2 + I_3 = \tfrac{1}{2}L^2$$

with $\vec{L}$ the total angular momentum vector $(L_{\rm x}, L_{\rm y}, L_{\rm z})$.

Then there are four isolating integrals of motion , namely the total energy E and the three components of the angular momentum $L_{\rm x}$, $L_{\rm y}$ and $L_{\rm z}$.

Types of orbits

For dynamical studies it is important to investigate the possible general types of orbits in the kind of potential considered. Here we look at orbits in triaxial potentials using the perfect ellipsoid.

It can be shown that the equations of motion become

$$E = 2(\tau + \beta) p_\tau^2 + \Phi_{\rm eff}(\tau)$$

with

$$p_\lambda = P^2 \dot{\lambda} \quad ; \quad p_\mu = Q^2 \dot{\mu} \quad ; \quad p_\nu = R^2 \dot{\nu}$$

$$\Phi_{\rm eff} = \frac{I_2}{\tau + \alpha} + \frac{I_3}{\tau + \gamma} - G(\tau)$$

Depending on the values of the integrals there are four general types of orbits.

Box orbits

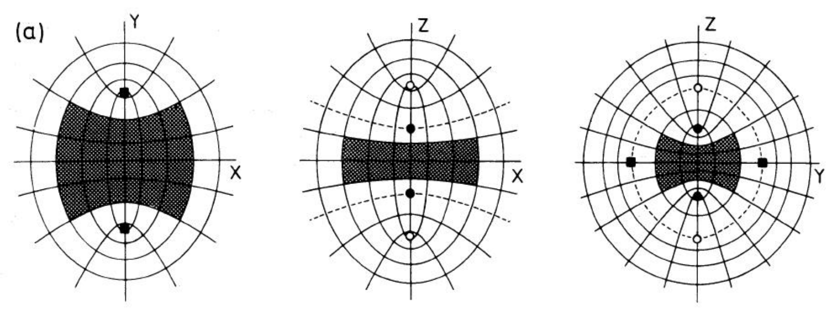

Inner long axis tube orbits

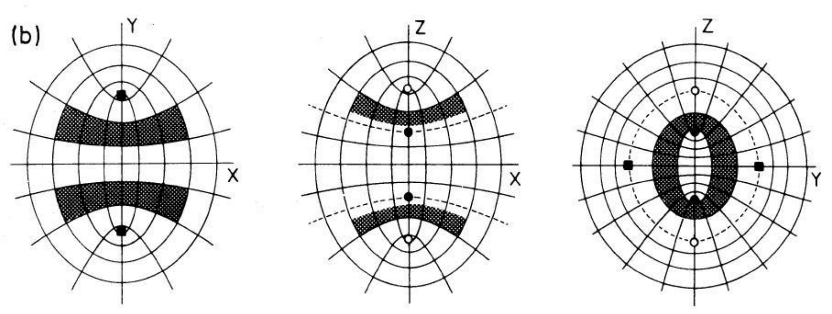

Outer long axis tube orbits

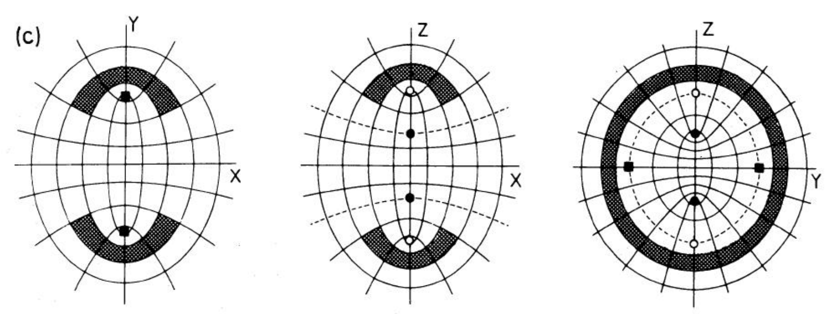

Short axis tube orbits

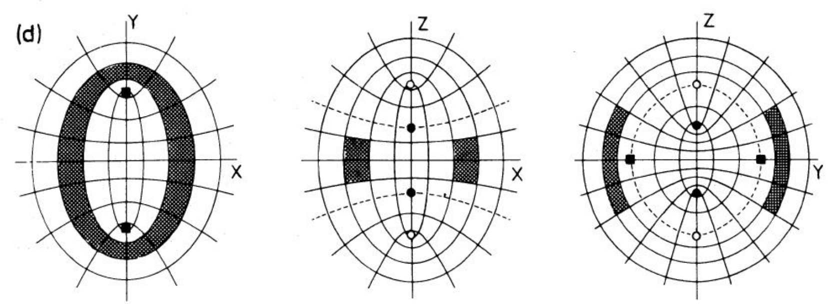

Next consider orbits in the (x, y)-plane.

This is for $\nu = -\gamma$ and $p_\nu^2/2R^2 = 0$.

It can be shown that for orbits in this plane we have

$$I_3 = 0$$

Then two types of orbits remain, which are versions of the orbits earlier, but now collapsed onto the (x, y)-axis.

These orbits turn out to be stable for perturbations perpendicular to this plane.

The two types of orbits that remain are butterflies (collapsed box orbits with $I_2 < 0$; left) and loops (collapsed short axis tubes with $I_2 > 0$; right), resp. inside or outside the foci.

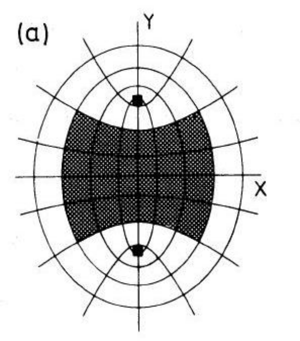

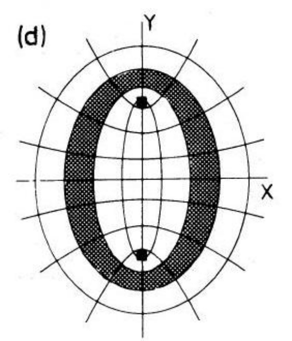

The orbits can be distinguished according to the integrals.

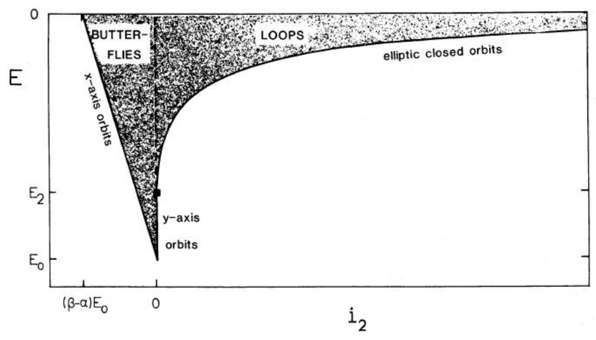

The limiting cases are x-axis orbits, y-axis orbits (which are unstable for x-perturbations) and elliptic closed orbits.

Then orbits in the (x, z)-plane.

Since $\mu = -\beta$ or $\nu = -\beta$

$$E - E_\circ = \frac{I_2}{\alpha - \beta} + \frac{I_3}{\gamma - \beta}$$

The fundamental orbits are again butterflies and loops.

The butterflies can either be stable (and then are collapsed box orbits) or unstable for perturbations in the y-direction. When stable they are collapsed box orbits.

The loops are all unstable.

Unstable butterfly

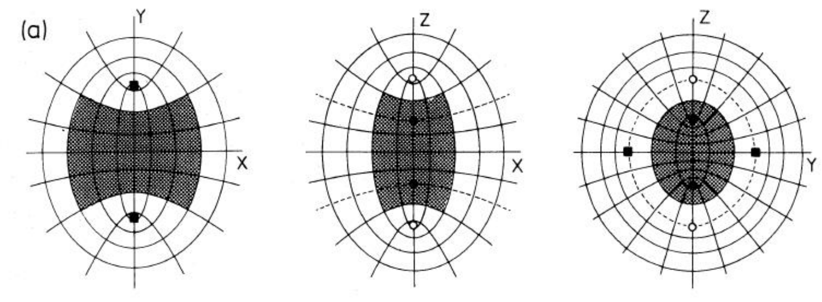

Unstable loop

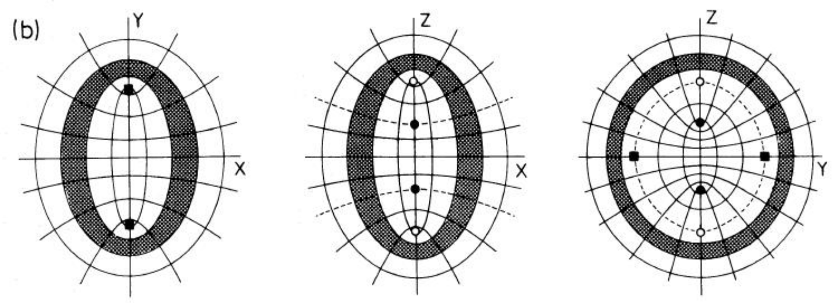

Classification of (x, z)-orbits (shaded is stable, dashed is unstable periodic orbits).

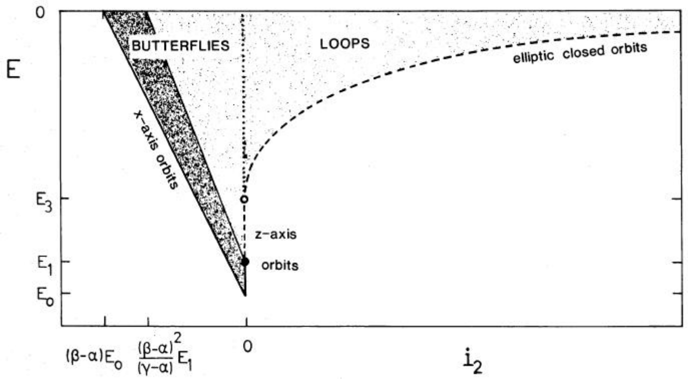

Orbits in the (y, z)-plane.

Now $\lambda = -\alpha$ or $\mu = -\alpha$.

Now we have

$$I_2 = 0$$

.
We have again butterflies and loops, but these can now be both stable and unstable.

The stable butterfly is a collapsed box orbits. There are two types of stable loops, either collapsed inner or outer long axis tubes.

Left the stable butterfly and on the right the two stable loops.

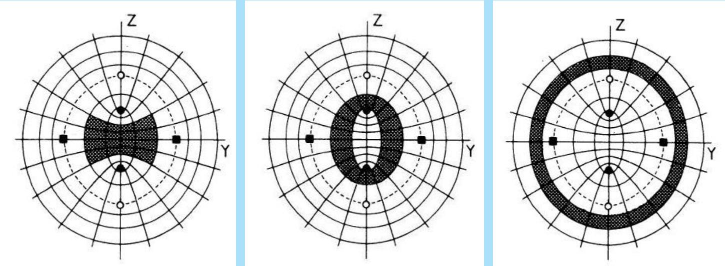

Unstable butterfly

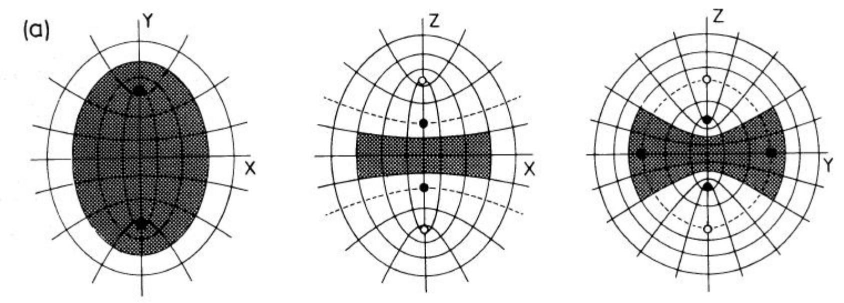

Unstable loop

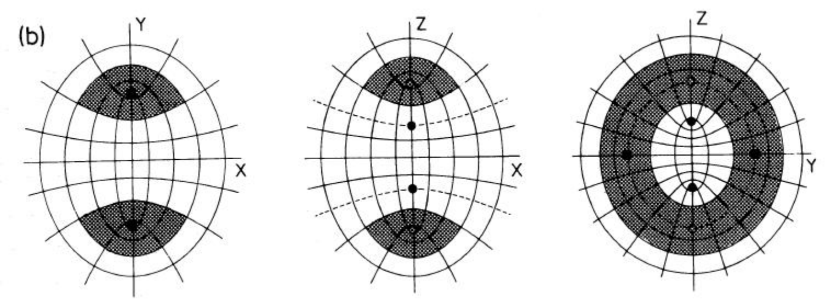

Classification of orbits

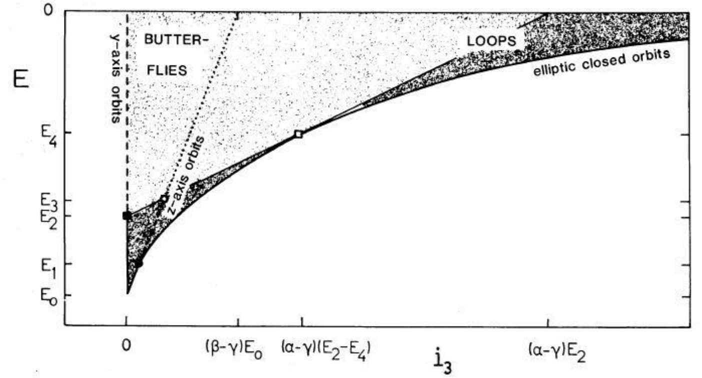

In the case of a prolate spheroid only two types of orbits are possible.
Here is the inner long axis tube.

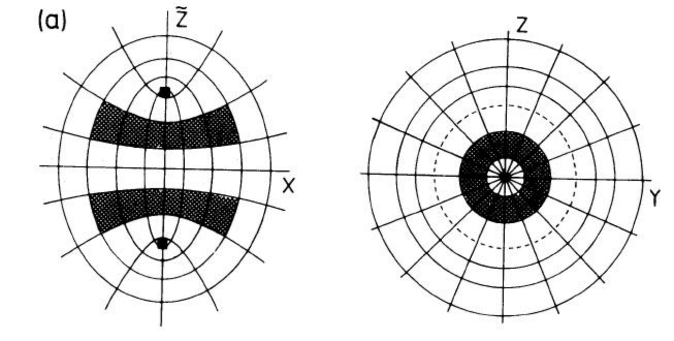

The vertical axis indicates that this is any meridional plane perpendicular to x.

The other possibility is the outer long axis tube

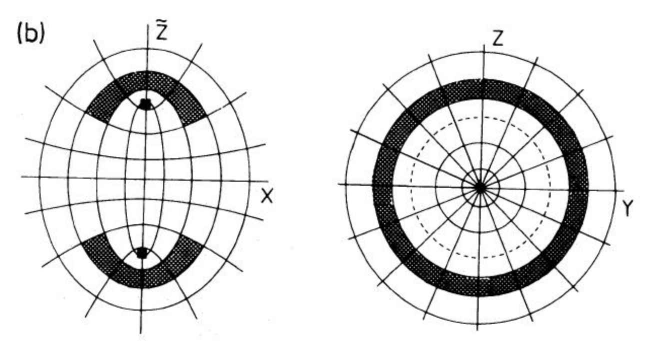

In the case of the oblate spheroid only short axis tube orbits are possible.

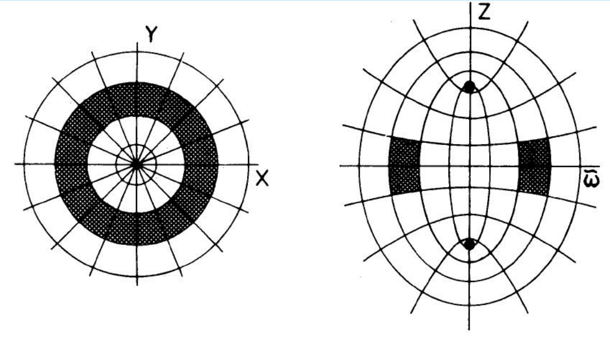

Dark matter

Solutions for isotropic models usually have gradients in M/L, while for triaxial models solutions with constant M/L are usually possible.

The manner to proceed and make progress then is to consider higher order moments of the observed velocity profiles.

For example Carollo et al.[22] show that at least three out of their four ellipticals must have dark haloes.

[22] C.M. Carollo, P.T. de Zeeuw, R.P. van der Marel, I.J. Danziger & E.E. Qian, 441, L25 (1995)

X-ray halos

X-ray emission at large radii can also be used to measure masses of large ellipticals and clusters.

Measure the X-ray emissivity distribution $\epsilon(r)$ from the distribution on the sky and the X-ray energy distribution.

Infer from the distribution of ϵ the density distribution of the gas $\rho_{\rm gas}(R)$ and the distribution of temperature $T(r)$.

Then the hydrostatic equation gives for the pressure P

$$\frac{dP}{dR} = -\frac{GM(<R)}{R^2}\rho_{\rm gas}(R)$$

The ideal gas equation gives

$$P = \rho_{\rm gas}\frac{kT}{\mu m_{\rm p}}$$

Then

$$M(<R) = -\frac{kT(R)R}{G\mu m_{\rm p}}\left[\frac{d\log\rho_{\rm gas}}{d\log R} + \frac{d\log T}{d\log R}\right].$$

Here are X-ray distributions in two clusters of galaxies.

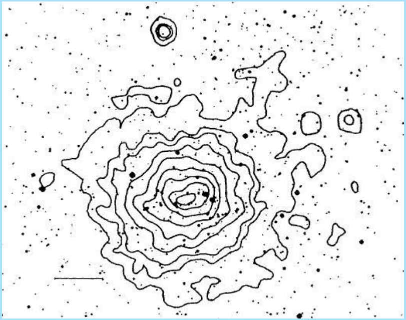

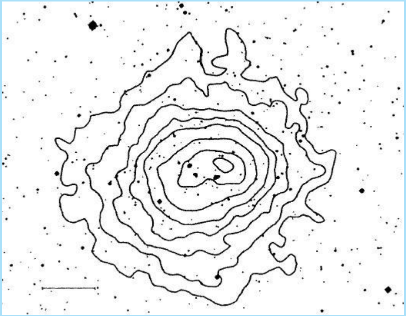

The next two graphs show the analysis of the giant elliptical M 87 in the center of the Virgo cluster[23].

[23] Fabricant & Gorenstein, Ap.J. 267, 535 (1983)

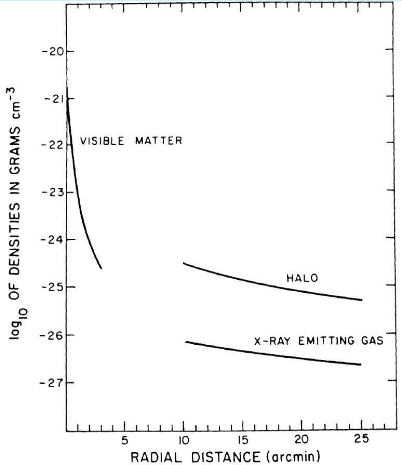
-20
-21
-22
-23
-24
-25
-26
-27
$\log_{10}$ OF DENSITIES IN GRAMS cm^{-3}
VISIBLE MATTER
HALO
X-RAY EMITTING GAS
5
10
15
20
25
RADIAL DISTANCE (arcmin)

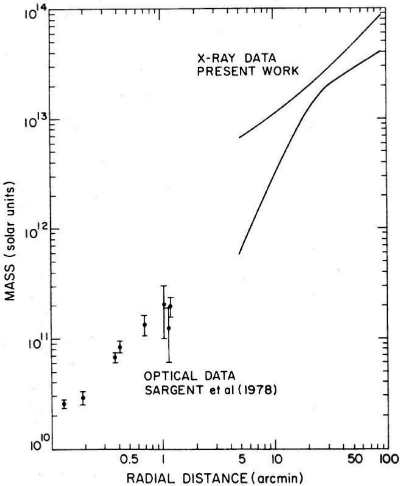
10^{14}
10^{13}
10^{12}
10^{11}
10^{10}
MASS (solar units)
X-RAY DATA
PRESENT WORK
OPTICAL DATA
SARGENT et al (1978)
0.5
1
5
10
50
100
RADIAL DISTANCE (arcmin)

Shells can also be used. Simulations show that their spacing depends on the mass profile.

Finally we can measure masses of whole clusters of galaxies.

The Virial Theorem $2T + \Omega \sim 0$ for equilibrium for a uniform, spherical distribution gives

$$2T = \sum mV^2 \sim M\langle V^2 \rangle \sim -\Omega \sim \frac{3GM}{5R}$$

Thus

$$M \sim \frac{R\sigma_{\mathrm{v}}^2}{G} \sim \left(\frac{R}{1\ \mathrm{Mpc}}\right)\left(\frac{\sigma_{\mathrm{v}}}{10^3\ \mathrm{km\ s^{-1}}}\right)^2 10^{15}\ \mathrm{M}_\odot$$

This indicates masses of up to 10^{15} $M_\odot$.

Nowadays also gravitational arcs can be used (e.g. in Abell 2218[24]).

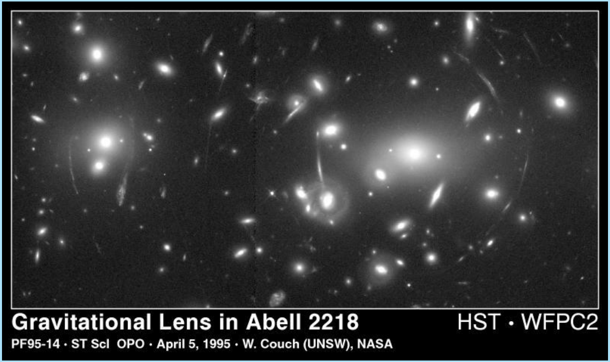

[24] J.P. Kneib et al., A.&A. 303, 27 (1995)

Here are the inferred distributions.